Spectrochimica Acta Part A: Molecular and Biomolecular Spectroscopy 99 (2012) 234–247

Contents lists available at SciVerse ScienceDirect

Spectrochimica Acta Part A: Molecular and Biomolecular Spectroscopy

journal homepage: www.elsevier.com/locate/saa

# Vibrational spectra, structural conformations, scaled quantum chemical calculations and NBO analysis of 3-acetyl-7-methoxycoumarin

Lynnette Joseph [a], D. Sajan [a,*], R. Reshmy [c], B.S. Arun Sasi [a], Y. Erdogdu [b], K. Kurien Thomas [c]

[a] Department of Physics, Bishop Moore College, Mavelikara, Alappuzha 690110, Kerala, India
[b] Department of Physics, Ahi Evran University, 40040 Kirsehir, Turkey
[c] Department of Chemistry, Bishop Moore College, Mavelikara, Alappuzha 690110, Kerala, India

## HIGHLIGHTS

- FT-Raman and FT-IR spectra of 3-acetyl-7-methoxycoumarin have been recorded and analyzed.
- Conformation analysis.
- The computed vibrational wavenumbers were seen to be in good agreement with the experimental data.

## GRAPHICAL ABSTRACT

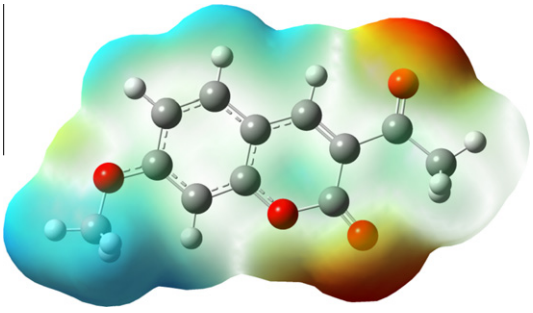

## ARTICLE INFO

*Article history:*
Received 16 February 2012
Received in revised form 20 May 2012
Accepted 5 July 2012
Available online 23 August 2012

*Keywords:*
3-acetyl-7-methoxycoumarin
FT-IR and FT-Raman spectra
PED
NBO
Electrostatic potential

## ABSTRACT

The powder form NIR-FT Raman and FT-IR spectra of 3-acetyl-7-methoxycoumarin (3A7MC) have been recorded in the regions 4000–400 and 3500–100 $cm^{-1}$, respectively. The equilibrium geometry, vibrational frequencies, band intensities, NMR spectra, NBO analysis and UV–Vis spectral studies of the most stable conformer have been calculated by density functional B3LYP method with the 6-311G(d,p) basis set. A complete vibrational analysis has been attempted on the basis of experimental infrared and Raman spectra, the calculated wavenumber and intensity of the vibrational bands and the potential energy distribution over the internal coordinates. Information about the size, shape, charge density distribution and site of chemical reactivity of the molecules has been obtained by mapping the electron density isosurface with electrostatic potential surfaces (ESP). Natural bond orbital analysis has been carried out to understand the nature of different interactions responsible for the electron delocalization and the intramolecular charge transfer between the orbitals ($n \rightarrow \pi^*$, $n \rightarrow \sigma^*$, $\pi \rightarrow \pi^*$).



## Introduction

Coumarins are an important group of naturally occurring compounds widely distributed in the plant kingdom such as Tonka bean, lavender, sweet clover grass, licorice, strawberries, apricots, cherries and cinnamon, and has been produced synthetically for many years for commercial uses [1]. Coumarin derivatives have been proven to function as anti-coagulants [2], antibacterial agents [3], antifungal agents [4], biological inhibitors [5], chemotherapeutics [6,7] and as bio-analytical reagents [8]. They are useful antioxidants and show antitumour activity [9] and cytotoxicity [10–15]. Members of this group display a broad range of applications, as fragrances, pharmaceuticals, additives to food, cosmetics, agrochemicals, optical brightening agents, dispersed fluorescent, tunable dye lasers, and possess varied biological activities like anthelmintic, hypnotic, insecticidal and anticoagulant properties [16–21]. The presence of a methyl group or a halogen atom or both in the ring system, often enhances the associated biological activity of coumarin derivatives [22].

* Corresponding author. Tel.: +91 9495043765; fax: +91 4792303230.
*E-mail address:* dsajand@gmail.com (D. Sajan).

1386-1425/$ - see front matter © 2012 Elsevier B.V. All rights reserved.
http://dx.doi.org/10.1016/j.saa.2012.07.084

In order to elucidate the relationship between biological activity and molecular structure, the knowledge of their conformational distribution, electronic structure and spectral properties are particularly important. In the vibrational analysis of polyatomic complex molecules, analysis of the assignment of vibrations is supported by quantum chemical calculations, because there are many couplings between vibrations. The vibrational spectra of 3-(bromoacetyl)coumarin [1], dihydro-, 6-methyl-, and 7-methylcoumarin, 6-methyl-4-bromomethylcoumarin, 7-methyl-4-bromomethylcoumarin, 6-chloro- and 7-chloro-4-bromomethylcoumarins, 3-acetyl-6-bromocoumarin, 3-acetyl-6-methylcoumarin, 4-bromomethylcoumarin, 7-amino-4-trifluoromethylcoumarin [23–31] molecules have been reported. According to previous literature, electronic absorption spectra for the parent coumarin and its derivatives have been reported by several authors [32–35]. The aim of this work is to predict the structural, electronic and spectroscopic properties of 3-acetyl-7-methoxycoumarin (Fig. 1) by applying experimental (NIR-FT Raman, FT-IR, NMR and UV–Vis spectra etc.) and theoretical (DFT-B3LYP level of theory with the use of standard 6-311G(d,p) basis set) methods. Though the crystal structure of the title compound, 3-acetyl-7-methoxycoumarin (3A7MC) has been reported [36], the vibrational spectral features of 3A7MC crystal have not been subject of detailed analysis so far. The UV–Vis spectroscopic behavior of 3A7MC was investigated with the aim of analyzing the influence of the substituent in the ring. Herein, the investigated results have been reported. The experimental and theoretical results support each other, and the calculations are valuable for providing a reliable insight into the vibrational spectra and the molecular properties.

## Experimental details

### *Synthesis of 3A7MC*

Commercially available AR grade of *m*-methoxysalicylaldehyde (0.05 mol, 7.724 g), ethylacetoacetate (0.055 mol, 7 mL), piperidine (one drop), glacialaceticacid (two drops) were taken in a stoppered flask and microwave irradiated for 15 s. The reaction mixture was then poured into cold water containing ice and filtered, washed with water and air-dried. Recrystallization from ethanol gave yellow needle shaped crystals. After about 5 days good quality crystals appeared and these crystals were then grown to large size crystals (yield 89%; m.p. 121 °C) of dimension $28 \times 7 \times 3$ mm within a period of 20 days by slow evaporation technique. Microwave radiation enhances the kinetics of Knoevenagel condensation by two to three folds over the conventional treatment [37]. The outstanding advantages of the green chemical approach including reduced reaction time, energy saving, exclusion of hazardous solvents etc. are extremely promising to the scientific as well as industrial community.

### *NMR, IR and Raman spectra*

Nuclear magnetic resonance (NMR) spectra were recorded to confirm the presence of various types of protons and carbons for the formation of the target compound. The NMR spectra of 3A7MC grown from ethanol water system were recorded using Brucker WM-400 (400 MHz) for $^{1}$H NMR and JEOL GSX (125 MHz) for $^{13}$C NMR spectrometers. The infrared spectrum of the sample was recorded between 4000 and 400 $cm^{-1}$ on a JASCO 400 FT-IR spectrometer, which was calibrated using polystyrene bands. The sample was prepared as a KBr disc. The FT-Raman spectrum of the sample was recorded between 3500 and 100 $cm^{-1}$ regions on a Bruker RFS 100/S FT-Raman Spectrometer instrument using 1064 nm excitation from an Nd:YAG laser. The detector is a liquid nitrogen cooled Ge detector. The UV–Vis absorption spectrum of the synthesized compound was recorded using SECOMOM ANTHELIE 70 M UV–Vis Spectrophotometer in the wavelength range 200–900 nm.

## Computational details

The quantum chemical calculation has been performed using the Becke-3-Lee–Yang–Parr (B3LYP) supplemented with the standard 6-311G(d,p) basis set, using the Gaussian 03 program [38] to calculate the optimized geometry and vibrational wavenumbers with their IR intensities and Raman scattering activities. The optimized geometry corresponding to the minimum on the potential energy surface have been obtained by solving the self-consistent field (SCF) equations iteratively. Harmonic vibrational wavenumbers have been calculated using analytic second derivatives to confirm the convergence to minima on the potential surface and to evaluate the zero-point vibrational energies without imposing any molecular symmetry constraints. It is a well known fact that *ab initio* calculations tend to overestimate the vibrational wavenumber with respect to the experimental ones. This is due to several reasons, for instance, the use of finite basis set, the incomplete implementation of the electronic correlation and the neglect of anharmonicity effects in the theoretical treatment. To improve the agreement between the predicted and observed wavenumber, the computed harmonic wavenumbers are usually scaled for comparison. In this work the force field was scaled according to the SQM procedure [39], the Cartesian representation of the force constants were transferred to a nonredundant set of local symmetry coordinates, chosen in accordance to the recommendations of

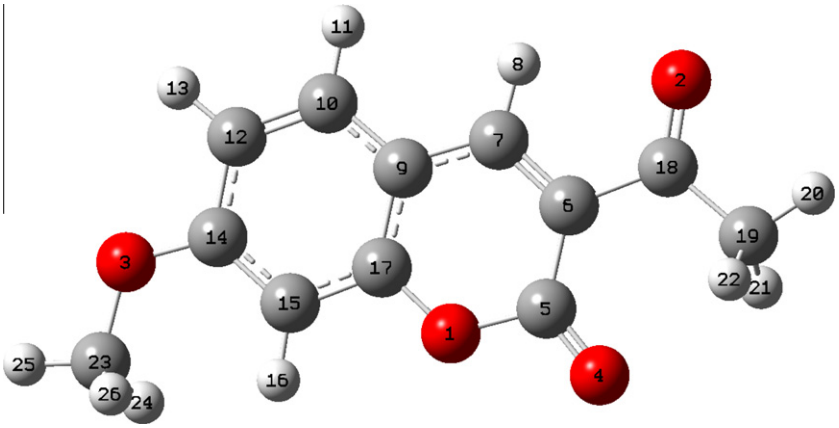


**Fig. 1.** Molecular structure and atomic numbering of 3-acetyl-7-methoxycoumarin.

Pulay et al. [40]. The scale factor calculation and characterization of the normal modes using potential energy distribution (PED) were done with the MOLVIB program 7.0 written by Sundius [41,42]. For the plots of simulated IR and Raman spectra, pure Lorentzian band shapes were used with a bandwidth (FWHM) of 10 $cm^{-1}$.

The prediction of Raman intensities was carried out by following the procedure outlined below. The Raman activities (Si) calculated by Gaussian 03 and adjusted during scaling procedure with MOLVIB were converted to relative Raman intensity (Ii) using the following relation from the basic theory of Raman scattering [43]

$$I_i = \frac{f(v_o - v_i)^4 S_i}{v_i[1 - \exp(\frac{-hcv_i}{kT})]} \quad (1)$$

where $v_o$ is the exciting frequency (in $cm^{-1}$ units), $v_i$ is the vibrational wavenumber of the $i$th normal mode, $h$ $c$ and $k$ are universal constants, and $f$ is the suitably chosen common scaling factor for all the peak intensities.

Isoelectronic molecular electrostatic potential surfaces (MEPSs) and electron density surfaces were calculated using 6-311G(d,p) basis set with (83,83,52) grid points with an average resolution of 0.333 Bohr. The structure resulting from the plot of electron density surface mapped with electrostatic potential surface depicts the shape, size, charge density and the site of chemical reactivity of a molecule. These surfaces were plotted by the computer software GaussView (Gaussian Inc., Pittsburgh, PA 15106, USA, 2003). Electronic transitions and oscillator strengths for 3A7MC molecule were calculated by time-dependent density functional theory (TD–DFT) using 6-311G(d,p) basis set and B3LYP functionals after taking into account the configuration interaction between singly excited states.

## Results and discussion

### NMR spectra

The nuclear magnetic resonance (NMR) spectrum was recorded to confirm the presence of various types of protons for the formation of the target compound. The recorded NMR spectrum is shown in Figs. 2a and 2b. A singlet at 3.29 ppm [3H] indicates the presence of methoxy linkage in the compound. Another singlet 1.63 ppm [3H] could be due to the presence acetyl group. The peak integral of multiplets in the aryl region $\delta$ 6.993–7.762 ppm that accounts for hydrogen atoms are well in agreement with suggested structure for the compound. The $^{13}C$ NMR spectrum of the compound is also in agreement with the number of carbon atoms present in the compound.

### Conformational analysis

The four conformers of 3A7MC molecule have been optimized at B3LYP/6-311G(d,p) level of theory and are shown in Fig. 3. The zero point corrected optimized energy of the conformers are predicted at −764.19653137 a.u. (conformer 1), −764.18604295 a.u. (conformer 2), −764.19427090 a.u. (conformer 3) and −764.18334222 a.u. (conformer 4). The relative energy of the conformers are determined at 0.0 kJ/Mol (conformer 1), 27.53 kJ/Mol (conformer 2), 5.93 kJ/Mol (conformer 3) and 34.62 kJ/Mol (conformer 4) for B3LYP/6-311 G(d,p) level of theory. As a result, the energy obtained for conformer-1 of 3A7MC molecule was found to be the global minimum.

The energy barrier of rotation around the $O_3$–$C_{14}$ and $C_6$–$C_{18}$ bond was calculated for the B3LYP with 6-311G(d,p) basis sets. The dihedral angles of $C_{15}$–$C_{14}$–$O_3$–$C_{23}$ (around $O_3$–$C_{14}$ bond) and $C_5$–$C_6$–$C_{18}$–$C_{19}$ (around $C_6$–$C_{18}$ bond) were varied from 0° to 360° by steps of 10°. The energy profile obtained from DFT method (Fig. 4) as a function of $\theta$ [$C_{15}$–$C_{14}$–$O_3$–$C_{23}$ and $C_5$–$C_6$–$C_{18}$–$C_{19}$] has shown a global minimum at 0° and global maximum at 90° which predicts that the conformer 1 of 3A7MC is the most stable one. This conformation and structure of 3A7MC obtained is used for vibrational spectral analysis.

### Molecular geometry

The molecular structure and atomic numbering of conformer-1 of 3A7MC is shown in Fig. 1. Calculated geometric parameters and definitions of the natural coordinates for the molecules are summarized in Supplementary Table S1 (Supplementary data). Optimized geometric parameters of 3A7MC are compared with XRD data of the molecule of 3A7MC. Calculated RMS shows that hybrid B3LYP functional gives quite good reproduction of experimental parameters.

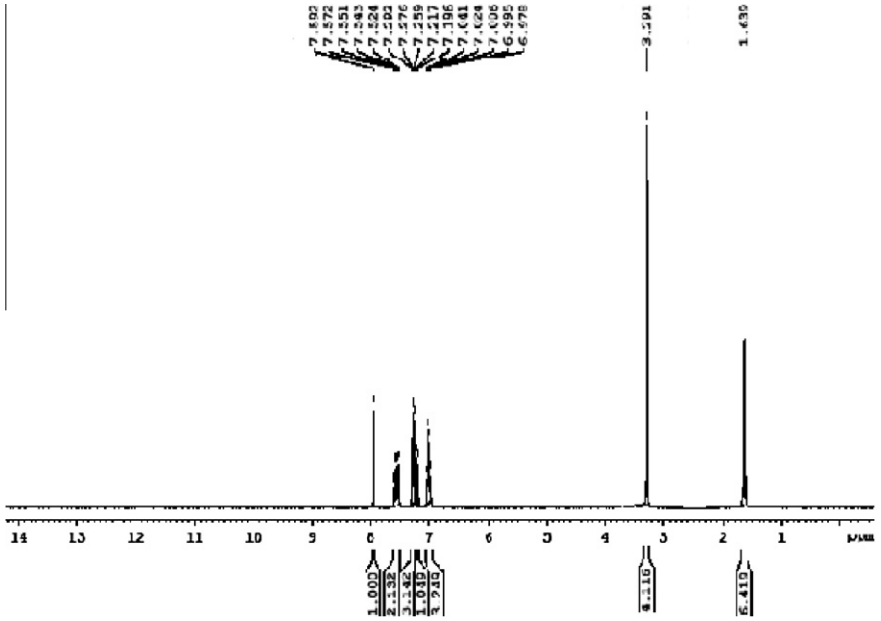

**Fig. 2a.** Experimental $^1H$ NMR spectrum of 3-acetyl-7-methoxycoumarin.

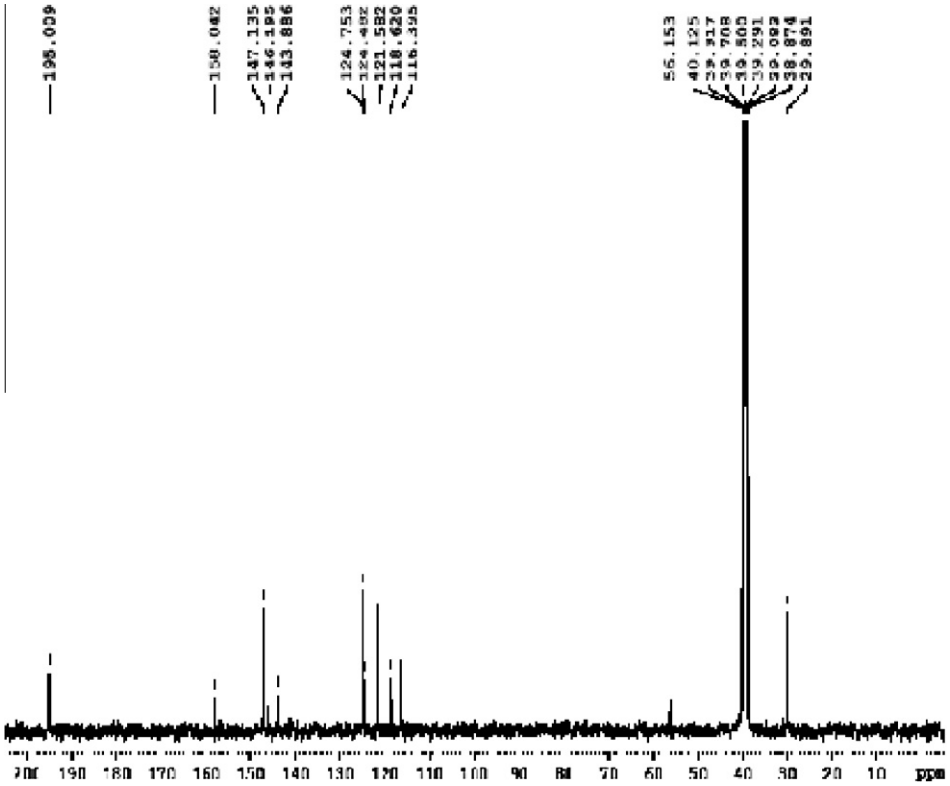


**Fig. 2b.** Experimental $^{13}C$ NMR spectrum of 3-acetyl-7-methoxycoumarin.

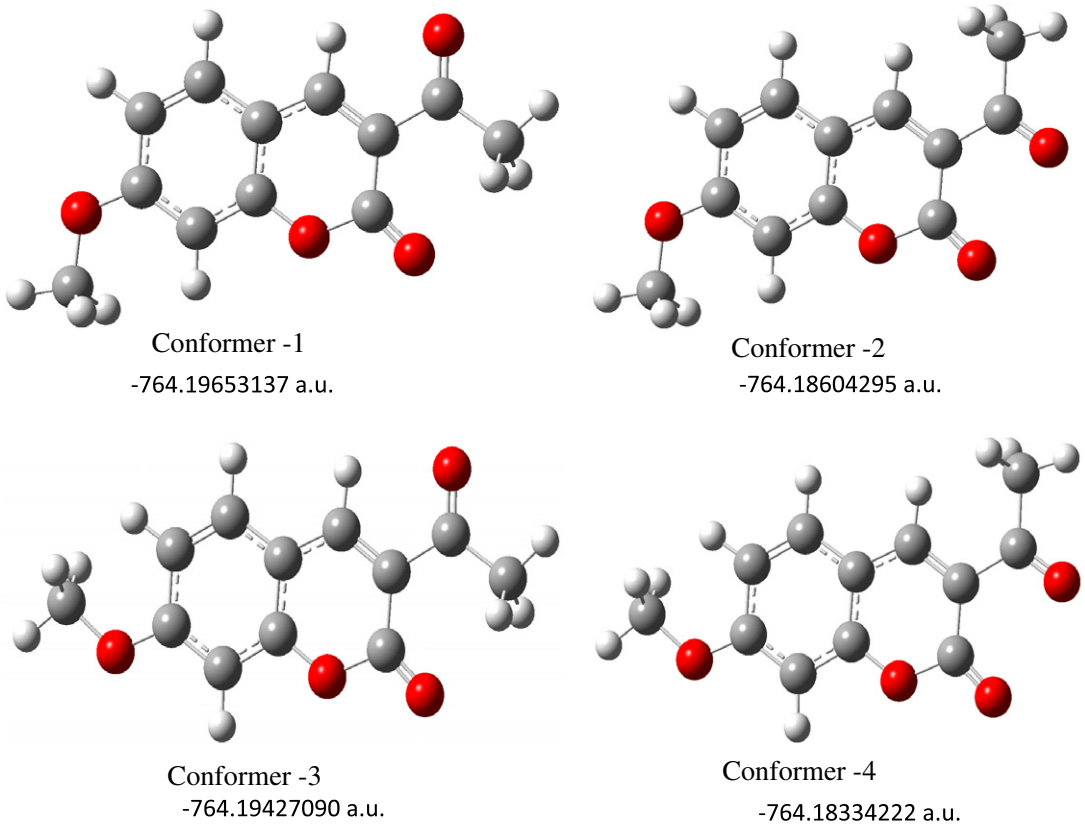


**Fig. 3.** Molecular structure of all conformers of 3-acetyl-7-methoxycoumarin.

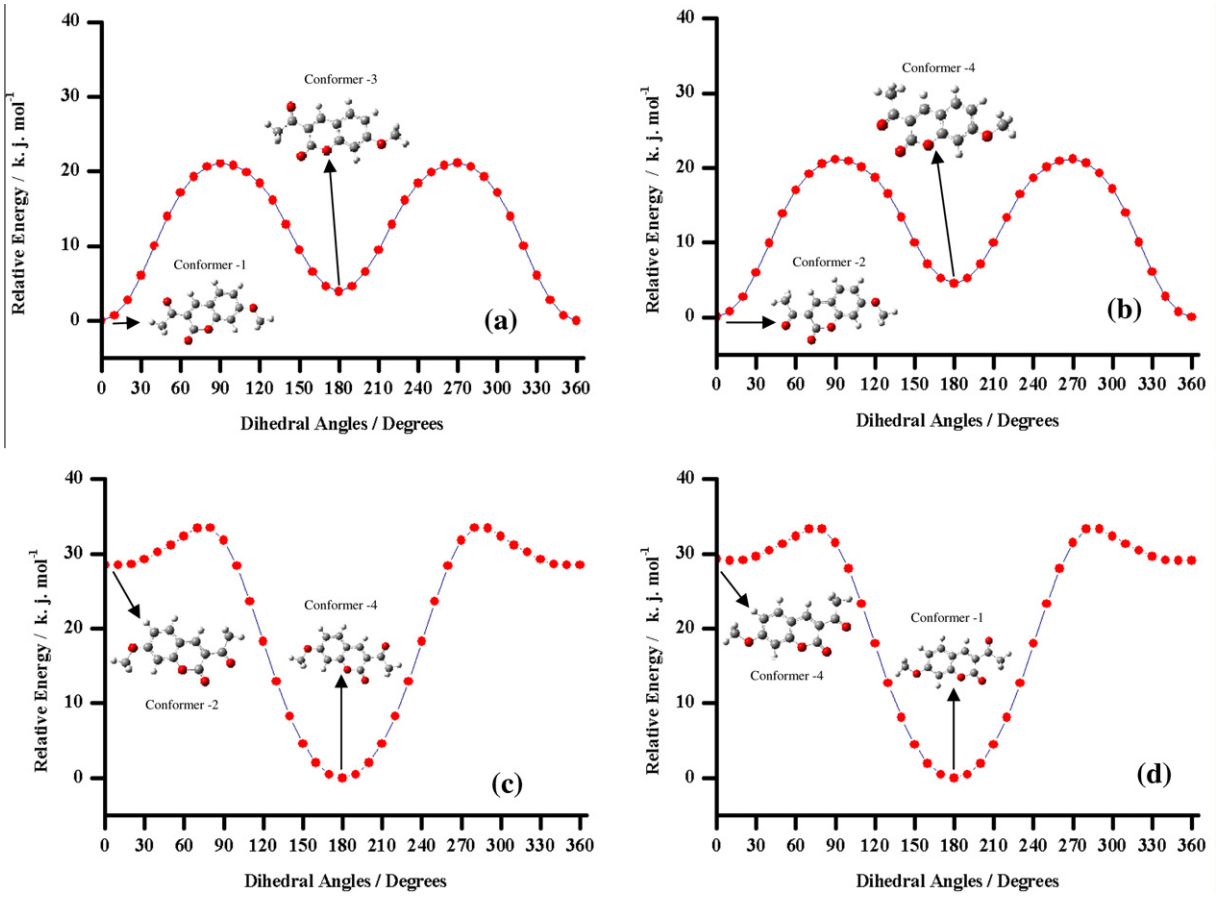


**Fig. 4.** Dihedral angles–energy curve for 3-acetyl-7-methoxycoumarin ($C_5$–$C_6$–$C_{18}$–$C_{19}$) for acetyl group (a and b) and $C_{15}$–$C_{14}$–$O_3$–$C_{23}$ for methoxy group (c and d)) by B3LYP/6-311G(d,p) level of theory.

**Table 1**
Second order perturbation theory analysis of Fock matrix in NBO basis.

| Lone pair | Occupancy | Donor–acceptor interaction | Hybrid (% *p* character) | $E(2)$[a] (kJ mol$^{-1}$) | $E$(j)–$E$(i)[b] (a.u.) | $F(i,j)$[c] (a.u.) |
|---|---|---|---|---|---|---|
| $LP_1\ O_1$ | 1.96089 | $n$ ($LP_1\ O_1$) → $\sigma^*(C_5–O_4)$ | $SP^{1.97}$(66.30) | 10.54 | 1.16 | 0.048 |
| | | $n$ ($LP_1\ O_1$) → $\sigma^*(C_5–C_6)$ | | 20.24 | 0.99 | 0.062 |
| | | $n$ ($LP_1\ O_1$) → $\sigma^*(C_9–C_{17})$ | | 29.65 | 1.07 | 0.078 |
| | | $n$ ($LP_1\ O_1$) → $\sigma^*(C_{15}–C_{17})$ | | 3.27 | 1.09 | 0.026 |
| $LP_2\ O_1$ | 1.73753 | $n$ ($LP_2\ O_1$) → $\pi^*(C_5–O_4)$ | $SP^{1.0}$(99.95) | 137.0 | 1.05 | 0.052 |
| | | $n$ ($LP_2\ O_1$) → $\pi^*(C_9–C_{17})$ | | 135.3 | 0.35 | 0.096 |
| $LP_1\ O_2$ | 1.97736 | $n$ ($LP_1\ O_2$) → $\sigma^*(C_6–C_{18})$ | $SP^{0.74}$(42.65) | 8.06 | 1.10 | 0.042 |
| | | $n$ ($LP_1\ O_2$) → $\sigma^*(C_{18}–C_{19})$ | | 7.27 | 1.08 | 0.039 |
| $LP_2\ O_2$ | 1.88913 | $n$ ($LP_2\ O_2$) → $\sigma^*(C_6–C_{18})$ | $SP^{1.0}$(99.94) | 82.95 | 0.68 | 0.104 |
| | | $n$ ($LP_2\ O_2$) → $\sigma^*(C_{18}–C_{19})$ | | 74.51 | 0.66 | 0.098 |
| $LP_1\ O_3$ | 1.96244 | $n$ ($LP_1\ O_3$) → $\sigma^*(C_{14}–C_{12})$ | $SP^{1.6}$(62.34) | 2.77 | 1.08 | 0.024 |
| | | $n$ ($LP_1\ O_3$) → $\sigma^*(C_{14}–C_{15})$ | | 30.95 | 1.10 | 0.081 |
| $LP_2\ O_3$ | 1.81646 | $n$ ($LP_2O_3$) → $\pi^*(C_{14}–C_{15})$ | $SP^{1.0}$(99.95) | 144.9 | 0.34 | 0.101 |
| $LP_1\ O_4$ | 1.97895 | $n$ ($LP_1\ O_4$) → $\sigma^*(C_5–O_1)$ | $SP^{0.71}$(41.47) | 3.23 | 0.98 | 0.025 |
| | | $n$ ($LP_1\ O_4$) → $\sigma^*(C_5–C_6)$ | | 14.2 | 1.13 | 0.056 |
| $LP_2\ O_4$ | 1.82836 | $n$ ($LP_2\ O_4$) → $\sigma^*(C_5–O_1)$ | $SP^{99.99}$(99.89) | 156.0 | 0.55 | 0.129 |
| | | $n$ ($LP_2\ O_4$) → $\sigma^*(C_5–C_6)$ | | 66.74 | 0.70 | 0.097 |

[a] $E(2)$ means energy of hyperconjugative interactions; *cf.* Eq. (2.0).
[b] Energy difference between donor and acceptor *i* and *j* NBO orbitals.
[c] $F(i,j)$ is the Fock matrix element between *i* and *j* NBO orbitals.

*NBO analysis*

The NBO analysis is already proved to be an effective tool for chemical interpretation of hyperconjugative interactions and electron density transfer from the filled lone pair electron. DFT level computation is used to investigate the various second-order interactions between the filled orbitals of one subsystem and vacant orbitals of another subsystem, which is a measure of the delocalization or hyperconjugation [44]. The main natural orbital interactions were analyzed with the NBO 5.0 program [45–47]. The hyperconjugative interaction energy was deduced from the second-order perturbation approach

$$E(2) = -n_\sigma \frac{\langle \sigma | F | \sigma \rangle^2}{\varepsilon_{\sigma^*} - \varepsilon_\sigma} = -n_\sigma \frac{F_{ij}^2}{\Delta E} \qquad (2)$$

**Table 2**
Definition of local symmetry coordinates (much like the natural internal coordinates) and the corresponding force constant (mdyne/Å) with scale factors used.

| No | Symbol | Definition | Scale factors | Force constants (mdyne/Å) |
|---|---|---|---|---|
| *Stretching* | | | | |
| 1–3 | CHr1 | $r_1$ | 0.923 | 5.534 |
| 4 | CHr2 | $r_2$, $r_3$ $r_4$ | 0.926 | 5.719 |
| 5–8 | CCr1 | $r_5$, $r_6$, $r_7$, $r_8$ | 0.989 | 8.032 |
| 9–13 | CC r2 | $R_9$, $R_{10}$, $R_{11}$, $R_{12}$, $R_{13}$ | 0.765 | 7.638 |
| 14–15 | $CH_3$ss | $(r_{14}+r_{15}+r_{16})/\sqrt{3}$, $(r_{17}+r_{18}+r_{19})/\sqrt{3}$ | 0.924 | 5.378 |
| 16–17 | $CH_3$ips | $(2r_{14}-r_{15}-r_{16})/\sqrt{6}$, $(2r_{17}-r_{18}-r_{19})/\sqrt{6}$ | 0.930 | 5.321 |
| 18–19 | $CH_3$ops | $(r_{15}-r_{16})/\sqrt{2}$, $(r_{18}-r_{19})/\sqrt{2}$ | 0.918 | 5.235 |
| 20–22 | OC | $Q_{20}$, $Q_{21}$, $Q_{22}$ | 0.829 | 12.397 |
| 23–24 | CC | $Q_{23}$, $Q_{24}$ | 0.944 | 4.393 |
| 25–27 | COr1 | $Q_{25}$, $Q_{26}$, $Q_{27}$ | 0.844 | 13.266 |
| *Bending* | | | | |
| 28 | Rtrid1 | $(\delta_{28}-\delta_{29}+\delta_{30}-\delta_{31}+\delta_{32}-\delta_{33})/\sqrt{6}$ | 0.711 | 1.502 |
| 29 | Rasyd1 | $(2\delta_{28}-\delta_{29}-\delta_{30}+2\delta_{31}-\delta_{32}-\delta_{33})/\sqrt{6}$ | 0.869 | 1.553 |
| 30 | Rasydo1 | $(\delta_{29}-\delta_{30}+\delta_{32}-\delta_{33})/2$ | 0.714 | 1.425 |
| 31 | Rtrid2 | $(\delta_{34}-\delta_{35}+\delta_{36}-\delta_{37}+\delta_{38}-\delta_{39})/\sqrt{6}$ | 0.504 | 1.487 |
| 32 | Rasyd2 | $(2\delta_{34}-\delta_{35}-\delta_{36}+2\delta_{37}-\delta_{38}-\delta_{39})/\sqrt{6}$ | 1.369 | 1.528 |
| 33 | Rasydo2 | $(\delta_{35}-\delta_{36}+\delta_{38}-\delta_{39})/2$ | 1.218 | 1.440 |
| 34 | bCH1 | $(\beta_{40}-\beta_{41})/\sqrt{2}$ | 0.875 | 0.515 |
| 35–37 | bCH2 | $(\beta_{42}-\beta_{43})/\sqrt{2}$, $(\beta_{44}-\beta_{45})/\sqrt{2}$, $(\beta_{46}-\beta_{47})/\sqrt{2}$ | 0.850 | 0.530 |
| 38 | $CCOr_1$ | $(\beta_{48}-\beta_{49})/\sqrt{2}$ | 0.699 | 1.236 |
| 39 | $CCOr_2$ | $(\beta_{50}-\beta_{51})/\sqrt{2}$ | 1.279 | 1.235 |
| 40 | CCb | $(\beta_{52}-\beta_{53})/\sqrt{2}$ | 0.960 | 1.366 |
| 41 | COb | $(\alpha_{54}-\alpha_{55})/\sqrt{2}$ | 0.572 | 1.309 |
| 42 | CCCb | $(2\beta_{56}-\alpha_{54}-\alpha_{55})/\sqrt{6}$ | 1.009 | 1.157 |
| 43–44 | $CH_3$sd | $(\alpha_{57}+\alpha_{58}+\alpha_{59}-\beta_{63}-\beta_{64}-\beta_{65})/\sqrt{6}$, $(\alpha_{60}+\alpha_{61}+\alpha_{62}-\beta_{66}-\beta_{67}-\beta_{68})/\sqrt{6}$ | 0.926 | 0.693 |
| 45–46 | $CH_3$ipb | $(2\alpha_{57}-\alpha_{58}-\alpha_{59})/\sqrt{6}$, $(2\alpha_{60}-\alpha_{61}-\alpha_{62})/\sqrt{6}$ | 0.899 | 0.576 |
| 47–48 | $CH_3$opb | $(\alpha_{58}-\alpha_{59})/\sqrt{2}$, $(\alpha_{61}-\alpha_{62})/\sqrt{2}$ | 0.944 | 0.582 |
| 49–50 | $CH_3$ipr | $(2\beta_{63}-\beta_{64}-\beta_{65})/\sqrt{6}$, $(2\beta_{66}-\beta_{67}-\beta_{68})/\sqrt{6}$ | 0.778 | 0.858 |
| 51–52 | $CH_3$opr | $(\beta_{64}-\beta_{65})/\sqrt{2}$, $(\beta_{67}-\beta_{68})/\sqrt{2}$ | 0.759 | 0.892 |
| 53 | OCb | $\beta_{69}$ | 0.975 | 1.397 |
| *Out-of-plane bending (wagging)* | | | | |
| 54 | gCH r1 | $\omega_{70}$ | 0.541 | 1.328 |
| 55 | gCarO | $\omega_{71}$ | 0.621 | 0.716 |
| 56 | gCC ar1 | $\omega_{72}$ | 0.567 | 0.474 |
| 57–59 | gCH ar2 | $\omega_{73}$, $\omega_{74}$, $\omega_{75}$ | 0.803 | 0.465 |
| 60–61 | gCO | $\omega_{76}$, $\omega_{77}$ | 0.938 | 0.712 |
| *Torsion* | | | | |
| 62–63 | Rpuck | $(\tau_{78}-\tau_{79}+\tau_{80}-\tau_{81}+\tau_{82}-\tau_{83})/\sqrt{6}$, $(\tau_{84}+\tau_{85}-\tau_{86}+\tau_{87}-\tau_{88}-\tau_{89})/\sqrt{6}$ | 1.027 | 0.377 |
| 64–65 | Rasyt | $(\tau_{78}-\tau_{80}+\tau_{81}-\tau_{83})/2$, $(\tau_{84}-\tau_{86}+\tau_{87}-\tau_{89})/2$ | 0.997 | 0.366 |
| 66–67 | Rasyto | $(-\tau_{78}+2\tau_{79}-\tau_{80}-\tau_{81}+2\tau_{82}-\tau_{83})/\sqrt{12}$, $(-\tau_{84}+2\ \tau_{85}-\tau_{86}-\tau_{87}+2\tau_{88}-\tau_{89})/\sqrt{12}$ | 1.334 | 0.543 |
| 68 | tC–CH3 | $(\tau_{90}+\tau_{91})/\sqrt{2}$ | 1.056 | 0.063 |
| 69 | tC–O | $(\tau_{92}+\tau_{93}+\tau_{94})/\sqrt{3}$ | 1.022 | 0.036 |
| 70 | tC–OCH3 | $(\tau_{95}+\tau_{96}+\tau_{97+}\ \tau_{98}+\tau_{99}+\tau_{100})/\sqrt{6}$ | 1.168 | 0.012 |
| 71 | tC–C | $(\tau_{101}+\tau_{102}+\tau_{103})/\sqrt{3}$ | 0.955 | 0.512 |
| 72 | tC–O | $(\tau_{104}+\tau_{105}+\tau_{106}+\tau_{107})/2$ | 0.780 | 0.021 |

where $\langle\sigma|F|\sigma\rangle^2$ or $F_{ij}^2$ is the Fock matrix element between the $i$ and $j$ NBO orbitals, $\varepsilon_\sigma$ and $\varepsilon_{\sigma^*}$ are the energies of σ and σ* NBO's, and $n_\sigma$ is the population of the donor σ orbital.

Table 1 shows the most important interactions between Lewis and non-Lewis orbitals with O lone pairs, the second order perturbation energy values, $E(2)$, corresponding to these interactions, and the overlap integral of each orbital pair. A very strong interaction has been observed between the p-type orbital containing the lone electron pair of $O_1$ and the neighbor $\pi^*(C_9–C_{17})$, $\pi^*(C_5–O_4)$ antibonding orbital of the benzene ring. This interaction is responsible for a pronounced decrease of the lone pair orbital occupancy 1.73753, than the other occupancy, and there is a possibility for hyperconjugation between $O_1$ and the benzene ring.

The contributions of the stabilization energies for the $n(LP_2\ O_1) \rightarrow \sigma^*(C_6–C_{18})$ [82.95 kJ mol$^{-1}$] and $n(LP_2\ O_1) \rightarrow \sigma^*(C_{18}–C_{19})$ [74.51 kJ mol$^{-1}$] charge transfers have higher values than the other delocalizations. An important contribution for the molecular stabilization is further given by $O_4$ through the overlap of its sp0.71 lone pair $n(LP_1\ O_4)$ with the $\sigma^*(C_5–C_6)$ orbital. The energy contribution of $LP_2\ O_4 \rightarrow \sigma^*(C_{19}–H_{20})$ value is 29.4 kJ mol$^{-1}$. These energy $E(2)$ values are chemically significant and can be used as a measure of the intramolecular C–H···O hydrogen bonding interaction between the oxygen lone pair and the antibonding orbitals.

The Mulliken population analysis in the 3A7MC molecule was calculated using the B3LYP/6-311G(d,p) level of theory. The charge distribution structure and chart of 3A7MC are shown in Supplementary Fig. S1 (Supplementary Material). The oxygen ($O_3$) and carbon ($C_6$) atom have large negative charges and behave as electron acceptor whereas the carbon atom $C_5$ acts as electron donor with large positive charge than the other carbon atoms. The result suggests that the atoms bonded to the carbon atoms and all oxygen atoms are electron acceptors and the charge transfer takes place from C to O. The carbon atom $C_{18}$ is more positive and $C_{19}$ is more negative than the other atoms due to electron-delocalization of π-electrons between the acetyl carbonyl and the pyrone, which increases the double bond character of the bond joining them.

*Vibrational spectral analysis*

The vibrational spectral assignments of 3A7MC have been carried out with the help of normal coordinate analysis. Internal coordinates have been described in Supplementary Table S2 according to Pulay's commendations [40]. The computed wavenumbers are selectively scaled according to the SQM procedure comprising a set of 11 transferable scale factors (Table 2) suggested by Rauhut and Pulay [48]. The detailed vibrational assignments of fundamental modes along with the calculated IR and Raman intensities and normal mode description (characterized by PED) are reported in Table 3. For visual comparison, the observed and simulated FT-IR and FT-Raman spectra are presented in Figs. 5 and 6, respectively.

*Acetyl group vibrations*

The acetyl group bonded to the pyrone ring gives rise to a series of characteristic bands corresponding to the carbonyl and methyl moieties. The carbonyl stretching wavenumber is very sensitive to the factors that disturb the nature of the carbonyl group and its precise wavenumber is a characteristic of the type of the carbonyl compound being studied. Particularly detailed correlations have been made for the carbonyl bond stretching wavenumber. The carbonyl stretching wavenumber has been most extensively studied by infrared spectroscopy. This multiply bonded group is highly polar ($>C^{\delta+}=O^{\delta-}$) and therefore gives rise to an intense infrared absorption band. The carbon oxygen double bond is formed by the $p_\pi$–$p_\pi$ bonding between carbon and oxygen. Because of the different electro negativities of carbon and oxygen atoms, the bonding electrons are not equally distributed between the two atoms. The following two resonance forms contribute to the bonding of the carbonyl group $>C{=}O \leftrightarrow C^{+}{-}O^{-}$. The lone pair of electrons on oxygen also determines the nature of the carbonyl group. The position of the C≡O stretching vibration is very sensitive to various factors such as the physical state, electronic effects by substituents, ring strains [49]. Consideration of these factors provides further information about the environment of the C=O group. The carbonyl stretching vibrations generally occurs as a strong absorption in the region from 1730–1645 $cm^{-1}$. This portion of the infrared spectrum is most useful because the position of the carbonyl absorption is quite sensitive to substitution effects and the geometry of the molecule. The sharp intense band in IR at 1683 $cm^{-1}$ and weak band at 1683 $cm^{-1}$ in Raman corresponds to acetyl carbonyl stretching vibrations. Reduction in intensity in the Raman band of the acetyl carbonyl stretching vibrations is probably caused by the conjugation of carbonyl bond with the ring [50]. The C=O in plane and out of plane bending modes are coupled with other modes (Table 3).

Methyl groups are generally referred to as electron donating substituents in the aromatic ring system [51]. The asymmetric and symmetric stretching modes of $CH_3$ group normally appear at 2965 and 2880 $cm^{-1}$ [52–54]. The asymmetric stretching mode is observed as a weak band as out of phase vibration (indicated as $CH_3$ ops in Table 3) at 2980 $cm^{-1}$ in IR and a weak band at 2974 $cm^{-1}$ in Raman. The weak Raman band at 2924 $cm^{-1}$ and a weak band in IR at 2930 $cm^{-1}$ are assigned to methyl symmetric stretching mode. The calculated wavenumbers of the above modes are 2978 $cm^{-1}$(100%) and 2930 $cm^{-1}$(99%) respectively for methyl asymmetric and symmetric modes. The lowering of the $CH_3$ stretching intensity in IR and the blue shifting of methyl stretching wavenumber is due to the hyperconjugation interaction between the σ(C–H) and $\sigma^*(C_{18}–O_2)$ bond. The NBO analysis clearly shows that there are 4.6, 21.4 and 7.1 kJ $mol^{-1}$ of energy involved in $\sigma(C_{19}–H_{20}) \rightarrow \sigma^*(C_{18}–O_2)$, $\sigma(C_{19}–H_{21}) \rightarrow \sigma^*(C_{18}–O_2)$ and $\sigma(C_{19}–H_{22}) \rightarrow \sigma^*(C_{18}–O_2)$ hyperconjugative interactions.

The asymmetric and symmetric bending vibrations of methyl groups normally appear in the region 1465–1410 and 1390–1370 $cm^{-1}$ respectively [52–55]. The medium band at 1433 $cm^{-1}$ in IR is attributed to the $CH_3$ asymmetric bending mode. The weak band around 1381 $cm^{-1}$ in IR corresponds to symmetric bending mode. The enhancement of IR intensity is due to the presence of carbonyl next to methyl in the acetyl group [56]. This is also in agreement with the calculated results. The relatively large value of IR intensity of the symmetric bending mode suggests a large positive charge localized on the hydrogen, which further supports the occurrence of hyperconjugation. The rocking vibrations of the $CH_3$ group in 3A7MC appear as mixed vibrations. These modes usually appear in the region 1070–1010 $cm^{-1}$ [52–54]. The intense band in IR spectra at 1185 $cm^{-1}$ is attributed to the $CH_3$ rocking mode, which is coupled with aromatic C=O stretching mode. The infrared band around 929 $cm^{-1}$ is due to the superposition of aromatic C–C stretching and $CH_3$ twisting mode, which is in agreement with the calculated results also.

*Methoxy group vibrations*

The methyl vibrational band positions are most consistent when this group is attached to other carbon atoms. When the $CH_3$ group is directly attached to an oxygen atom, the C–H stretching and bending bands can shift position due to electronic effects [56]. This causes the O–$CH_3$ stretching bands to be spread over a larger region than that of the C–$CH_3$ group. For the aryl methoxy group, the methyl stretching bands occur in the region 3000–2815 $cm^{-1}$ [56–59]. The observed bands at 3017 $cm^{-1}$ in the Raman spectrum and 3016 $cm^{-1}$ in the IR are assigned to methyl asymmetric stretching vibrations. The symmetric stretching mode of methoxy group of 3A7MC is observed as a weak band in IR and Raman spectra around 2855 and 2853 $cm^{-1}$ respectively. The asymmetric stretching and symmetric stretching modes of methoxy group vibrations are calculated to be 3020 $cm^{-1}$(42%) and 2924 $cm^{-1}$(90%) respectively. The lowering of the IR intensity of the $CH_3$ stretching and the blue-shifting of methyl stretching modes is due to electronic effects resulting from induction of the methyl group with the aromatic ring system from lone pair oxygen atoms to the antibonding $\sigma^*$(C–H) bonds [56].

The asymmetric bending vibrations of methoxy groups normally appear in the region 1460 $cm^{-1}$ [52–54]. The medium band at 1466 $cm^{-1}$ in IR and strong band at 1474 $cm^{-1}$ in Raman are assigned to the methoxy asymmetric bending mode. The weak band around 1445 $cm^{-1}$ in Raman spectra is due to the symmetric bending mode. The higher wavenumber corresponds to methyl in phase umbrella mode and the lower one arises from the out of phase umbrella mode of $CH_3$ group. This is in agreement with the calculated results also. The rocking vibration of the $CH_3$ group in 3A7MC is appearing as mixed vibrations. The mixing of C–O stretch and $CH_3$ rock, as predicted by computations, result in the weak band at 1128 $cm^{-1}$ in Raman, which is also strongly coupled with aromatic C–H in-plane bending mode. The intensity enhancement is owing to increased conjugation with the ring-system. The calculated hyperconjugative interactions between $LP_1(O_3) \rightarrow \sigma^*(C_{23}–H_{24}/C_{23}–H_{25})$ and $LP_2(O_3) \rightarrow \sigma^*(C_{23}–H_{24}/C_{23}–H_{25})$ are 12.19 and 21.67 kJ $mol^{-1}$ respectively, show the magnitude of conjugation with the aryl ring.

*Ring system vibrations*

The aromatic C–H stretching [23–31,54–56] vibrations are generally observed in the region 3000–3100 $cm^{-1}$. In this region, the bands are not affected by the nature of the substituents [57]. Hence in the present investigation, the IR bands at 3120 $cm^{-1}$, 3051 $cm^{-1}$, and Raman bands at 3084 $cm^{-1}$, 3067 $cm^{-1}$ have been assigned to C–H stretching vibrations. Most of the C–H stretching modes are found to be weak which is due to the charge transfer from the hydrogen atoms to the carbon atoms. DFT calculated wavenumbers are in good agreement with the experimental values. A comparison with the results from the normal mode of coumarin shows that the

**Table 3**
Vibrational assignment of 3A7MC by normal mode analysis based on SQM force field calculations.

| Mode no. | Calculated wavenumbers ($cm^{-1}$) | | Observed wavenumbers ($cm^{-1}$) | | IR intensity | Raman intensity | Characterization of normal modes with PED (%) |
|---|---|---|---|---|---|---|---|
| | Unscaled | scaled | FTIR | Raman | | | |
| $\nu_1$ | 3228 | 3106 | 3120w | – | 0.31 | 1.60 | $\nu CH_{R2}$(99) |
| $\nu_2$ | 3206 | 3085 | – | 3084w | 0.50 | 4.00 | $\nu CH_{R2}$(99) |
| $\nu_3$ | 3180 | 3061 | – | 3067w | 0.71 | 1.80 | $\nu CH_{R2}$(99) |
| $\nu_4$ | 3174 | 3051 | 3051w | – | 0.15 | 0.90 | $\nu CH_{R1}$(96) |
| $\nu_5$ | 3146 | 3036 | – | – | 3.99 | 3.00 | $CH3_{ips1}$(61), $CH3_{ops2}$(26) |
| $\nu_6$ | 3146 | 3020 | 3016w | 3017w | 6.23 | 4.50 | $CH3_{ops2}$(42),$CH3_{ips1}$(39), $CH3_{ips2}$(14) |
| $\nu_7$ | 3107 | 2978 | 2980w | 2974w | 0.84 | 1.30 | $CH3_{ops1}$(100) |
| $\nu_8$ | 3080 | 2965 | 2956w | – | 7.27 | 2.60 | $CH3_{ips2}$(74), $CH3_{ops2}$(25) |
| $\nu_9$ | 3048 | 2930 | 2924w | 2930w | 0.41 | 4.90 | $CH3_{ss1}$(99) |
| $\nu_{10}$ | 3016 | 2924 | 2855w | 2853w | 4.32 | 1.90 | $CH3_{ss2}$(90) |
| $\nu_{11}$ | 1815 | 1731 | 1731w | 1729m | 0.64 | 0.20 | $\nu CO_{R1}$ (80) |
| $\nu_{12}$ | 1752 | 1683 | 1683vs | 1683w | 100 | 4.90 | $\nu$CO(74) |
| $\nu_{13}$ | 1656 | 1608 | 1604s | 1604vs | 28.6 | 1.20 | $\nu CC_{R2}$(59), $\delta CH_{R2}$(15), $R_{asyd}$(11) |
| $\nu_{14}$ | 1628 | 1576 | 1572w | 1570vs | 84.5 | 34.0 | $\nu CC_{R1}$(42), $\nu CC_{R2}$ (28) |
| $\nu_{15}$ | 1576 | 1554 | – | – | 43.3 | 16.0 | $\nu CC_{R1}$(42), $\nu CC_{R2}$ (22) |
| $\nu_{16}$ | 1537 | 1540 | 1540vs | – | 3.98 | 0.80 | $\delta CH_{R1}$ (33), $\nu CC_{R2}$ (30), $\nu CC_{R1}$(14) |
| $\nu_{17}$ | 1504 | 1495 | – | 1474s | 87.6 | 100 | $CH3_{asydi2}$(33), $CH3_{asydo2}$(21) |
| $\nu_{18}$ | 1495 | 1474 | 1466m | – | 3.21 | 0.01 | $CH3_{asydo2}$(73), $CH3_{asydi2}$(23) |
| $\nu_{19}$ | 1482 | 1440 | – | 1445w | 9.29 | 1.20 | $CH3_{syd2}$(73) |
| $\nu_{20}$ | 1466 | 1428 | 1433m | – | 4.63 | 4.80 | $CH3_{asydo1}$(93) |
| $\nu_{21}$ | 1456 | 1412 | – | 1410w | 10.2 | 1.80 | $\nu CC_{R2}$(44), $\delta CH_{R2}$(19) |
| $\nu_{22}$ | 1451 | 1381 | 1381w | – | 1.99 | 4.10 | $H3_{asydi1}$(82) |
| $\nu_{23}$ | 1403 | 1355 | 1354w | 1355s | 2.95 | 2.40 | $\nu CC_{R1}$(24), $\nu CC_{R2}$(21), $CH3_{syd1}$(11) |
| $\nu_{24}$ | 1397 | 1303 | 1296w | – | 3.38 | 0.90 | $CH3_{syd1}$(61), $\nu CC_{R1}$(13) |
| $\nu_{25}$ | 1379 | 1282 | 1279w | 1282w | 6.03 | 2.60 | $\nu CC_{R2}$(34), $\nu CC_{R1}$(31), $\delta CH_{R1}$(11) |
| $\nu_{26}$ | 1313 | 1254 | 1248vs | – | 26.2 | 64.0 | $\delta CH_{R1}$(11), $R_{trid2}$(15), $\nu CC_{R2}$(14), $\nu CC_{R1}$(10), $\nu CO_{R2}$(10) |
| $\nu_{27}$ | 1293 | 1229 | – | 1232w | 5.19 | 5.90 | $\nu CC_{R2}$(21), $\nu CC_{R1}$(18), $\nu CO_{R2}$(15), $\nu$CC(13) |
| $\nu_{28}$ | 1278 | 1218 | – | 1206m | 12.2 | 13.0 | $\delta CH_{R2}$(37), $R_{trid1}$(12), $\nu CC_{R2}$(11), |
| $\nu_{29}$ | 1226 | 1190 | 1185s | – | 8.08 | 1.40 | $CH3_{Roko1}$(32), $\nu CO_{R1}$(7), $CH3_{Roki1}$(10) |
| $\nu_{30}$ | 1223 | 1141 | 1137w | 1140w | 34.1 | 8.20 | $\delta CH_{R1}$(23), $\nu CC_{R2}$(15), $\nu$CC(11) |
| $\nu_{31}$ | 1191 | 1122 | – | 1128w | 1.51 | 4.30 | $\delta CH_{R2}$(30), $CH3_{Roko2}$(21), $\nu CO_{R1}$(12) |
| $\nu_{32}$ | 1170 | 1091 | 1089w | 1095w | 87.0 | 8.00 | $CH3_{Roki2}$(69), $CH3_{Roko2}$(24) |
| $\nu_{33}$ | 1144 | 1073 | 1073w | 1075w | 0.93 | 0.10 | $\delta CH_{R2}$(53), $\nu CC_{R2}$(16) |
| $\nu_{34}$ | 1097 | 1058 | – | – | 1.28 | 4.30 | $\nu CC_{R1}$(26), $\nu CO_{R1}$(15), $\delta CH_{R2}$(13) |
| $\nu_{35}$ | 1055 | 1037 | 1036m | – | 0.40 | 1.20 | $CH3_{Roko1}$(36),$OC_{wag}$ (30) |
| $\nu_{36}$ | 1049 | 1022 | – | – | 0.83 | 1.80 | $\nu$CO(68), $\nu CC_{R2}$(17) |
| $\nu_{37}$ | 1003 | 994 | 999m | 995m | 3.75 | 1.60 | $CC_{wag}$(36), tCOC(29) |
| $\nu_{38}$ | 994 | 965 | 957w | 973m | 0.90 | 18.0 | $R_{trid2}$(25), $\nu CO_{R1}$(19), $\nu CC_{R2}$(18), $\delta CH_{ph2}$(10) |
| $\nu_{39}$ | 988 | 928 | 929w | – | 2.11 | 0.60 | $CH3_{Roki1}$(40), $\nu$CC (25) |
| $\nu_{40}$ | 965 | 904 | – | – | 17.6 | 3.80 | $R_{wag(}$(78),$CCH_{wag(}$(12) |
| $\nu_{41}$ | 931 | 893 | – | 884w | 0.08 | 0.10 | $\nu CO_{R1}$(42), $R_{trid1}$(14), $\delta CO_{R1}$ (13) |
| $\nu_{42}$ | 858 | 870 | 861w | – | 7.72 | 9.70 | $R_{wag(}$(62),$R_{puck2}$(19) |
| $\nu_{43}$ | 838 | 841 | – | – | 0.07 | 23.0 | $\nu CC_{R1}$(26), $\nu CC_{R2}$(24), $\nu$CC(14) |
| $\nu_{44}$ | 828 | 810 | 804w | – | 17.8 | 13.0 | $R_{wag(}$(76), $R_{asyto}$(10) |
| $\nu_{45}$ | 823 | 787 | 787w | – | 1.66 | 0.10 | $R_{trid1}$(23), $\nu CO_{R1}$(18), $R_{trid2}$(14) |
| $\nu_{46}$ | 783 | 779 | 768w | 774w | 0.26 | 42.0 | $OC_{wag}$(38), $R_{puck1}$(33), $CC_{wag}$(28) |
| $\nu_{47}$ | 738 | 720 | 718m | 715w | 1.44 | 0.70 | $\nu CC_{R1}$(26), $R_{asyto}$(14),$R_{trid2}$(10) |
| $\nu_{48}$ | 732 | 691 | 692w | – | 1.09 | 0.50 | $R_{puck}$(58) |
| $\nu_{49}$ | 654 | 678 | 665w | – | 0.18 | 18.0 | $CO_{wag}$(40), $R_{asyto2}$(19) |
| $\nu_{50}$ | 648 | 641 | – | 641m | 2.94 | 0.10 | $R_{asydo2}$(41), $\delta CH_{R!}$(23) |
| $\nu_{51}$ | 627 | 615 | – | 620w | 2.14 | 15.0 | $\delta$CCO (23), $R_{trid1}$(14), $\nu CC_{R1}$(11), |
| $\nu_{52}$ | 596 | 584 | 596w | - | 9.79 | 6.40 | $OCC_{wag(}$45), $CH3_{Roko1}$(21) |
| $\nu_{53}$ | 592 | 542 | – | – | 0.10 | 5.80 | $R_{asydo1}$(33), $\delta$CCO (12), $R_{asydi2}$(12) |

(*continued on next page*)

**Table 3** (*continued*)

| Mode no. | Calculated wavenumbers ($cm^{-1}$) | | Observed wavenumbers ($cm^{-1}$) | | IR intensity | Raman intensity | Characterization of normal modes with PED (%) |
|---|---|---|---|---|---|---|---|
| | Unscaled | scaled | FTIR | Raman | | | |
| $\nu_{54}$ | 529 | 518 | 500w | – | 0.02 | 0.90 | $\delta$COC (25), $R_{asydi2}$(21), $\delta$CCO (25) |
| $\nu_{55}$ | 485 | 458 | 458w | – | 1.49 | 3.60 | $R_{asydi1}$(35), $\delta CO_{R2}$(17), $R_{asydi2}$(10) |
| $\nu_{56}$ | 470 | 451 | – | 444w | 11.4 | 0.40 | $R_{asyto2}$(31), $R_{asytri2}$(19), $R_{asyto1}$(13) |
| $\nu_{57}$ | 437 | 420 | – | – | 0.30 | 1.10 | $R_{asydi1}$(21), $R_{asydo2}$(17), $\delta$CCO (15), $\delta CO_{R1}$(10) |
| $\nu_{58}$ | 434 | 400 | – | – | 0.36 | 9.10 | $R_{asyto1}$(36), tCOC(21) |
| $\nu_{59}$ | 383 | 363 | – | – | 0.28 | 13.0 | $\delta$CCO (43), $\delta CO_{R1}$(16) |
| $\nu_{60}$ | 342 | 342 | – | – | 0.41 | 0.80 | $\delta$CCO (18), $\delta CO_{R1}$(13),$R_{asydi1}$(12) |
| $\nu_{61}$ | 317 | 313 | – | 310w | 0.47 | 1.50 | $R_{asyto1}$(24),$CO_{wag}$ (21) |
| $\nu_{62}$ | 298 | 298 | – | – | 2.03 | 1.50 | $\delta$CCO (21), $R_{asydi2}$(19) |
| $\nu_{63}$ | 269 | 285 | – | – | 1.48 | 8.20 | $R_{asyto2}$(23), $R_{puck1}$(20),tCOC(14) |
| $\nu_{64}$ | 230 | 224 | – | 225w | 0.65 | 1.30 | tCOC(31), $R_{asyto2}$(21), $R_{puck1}$(16), |
| $\nu_{65}$ | 209 | 196 | – | – | 1.64 | 23.0 | $\delta CC_{R1}$(34), $\delta CO_{R1}$(34), $\delta COC_{R1}$(18) |
| $\nu_{66}$ | 190 | 190 | – | 193w | 0.07 | 1.30 | $R_{asyti2}$(37), $CO_{wag}$ (14) |
| $\nu_{67}$ | 169 | 171 | – | 153w | 0.00 | 4.40 | tCOH(73), $CH3_{Rocko1}$(14) |
| $\nu_{68}$ | 143 | 135 | – | 132w | 0.09 | 3.30 | $\delta CC_{R1}$(37), $\delta CO_{R2}$(20), $R_{asydi2}$(10) |
| $\nu_{69}$ | 113 | 111 | – | – | 0.94 | 2.30 | tCOC(57,) tCOCH(13) |
| $\nu_{70}$ | 91 | 91 | – | 84s | 0.09 | 4.70 | $R_{asyti1}$(32),$R_{puck1}$(26), tCOC(21) |
| $\nu_{71}$ | 49 | 49 | – | – | 1.01 | 0.00 | tCCCO (20), $R_{asytri1}$(18) |
| $\nu_{72}$ | 42 | 37 | – | – | 0.07 | 0.90 | $R_{asyto1}$(30), tCCCO (20), $R_{asytri1}$(16) |

vs: Very strong; ms: medium strong; s: strong; w: weak; vw: very weak.
$\nu$: Stretching; R1: ring1; R2: phenyl ring2; t: torsion; g: gauche; wag: wagging; ss: symmetric stretching; as: asymmetric stretching; sd: symmetric deformation; ips: in plane stretching; ops: out of plane stretching; ipb: in plane bending; opb: out of plane bending; sb: symmetric bending; rck: rocking; ipr: in plane rocking; opr: out of plane rocking; R: ring; trid: trigonal deformation; asyd: asymmetric deformation; asydo: out of plane asymmetric deformation; puck: puckering; asyt: asymmetric torsion; asyto: out of plane asymmetric torsion; sc: scissoring.

aromatic C–H stretching vibrations around 3050 $cm^{-1}$ remain unaltered by methoxy and acetyl substitution [23–31]. The C–H in-plane bending vibrations appear in the region 1300–1000 $cm^{-1}$ and C–H out of plane bending vibrations in the range of 1000–675 $cm^{-1}$. The bands corresponding to the C–H in-plane bending vibrations are identified in 3A7MC at 1248, 1137, 1073 $cm^{-1}$ in infrared spectra and 1206, 1140, 1075 $cm^{-1}$ in Raman spectra. The corresponding calculated modes are dominated by C–H in plane bending and coupled with C–C stretching. The C–H out-of-plane bending vibrations and ring breathing and ring puckering vibrations are shown in Table 3.

The carbonyl stretching vibrations are found in the region 1750–1700 $cm^{-1}$ [52–54]. The weak IR band at 1731 $cm^{-1}$ and the medium band 1727 $cm^{-1}$ in Raman spectrum corresponds to the carbonyl vibration in the pyrone ring [23–31]. The corresponding theoretical band with the comparable intensity is at 1731 $cm^{-1}$. In 3A7MC, the C═O bond in the lactone part is conjugated with $C_7$═$C_6$ and $C_9$═$C_{17}$ double bonds. The increase in single bond character due to conjugation lowers the wavenumber of carbonyl and double bond absorptions. In the present study, the carbonyl vibrational wavenumbers in the lactone part $C_5$═$O_4$ stretching have been lowered to different extents due to conjugation. The orbital interaction energy for $n(LP_2\ O_4) \rightarrow \sigma^*(C_5–O_1)$ is 156.0 kJ $mol^{-1}$ and $n(LP_2\ O_1) \rightarrow \pi^*(C_5–C_6)$ is 66.74 kJ $mol^{-1}$ which are higher values than the other delocalizations. These charge transfer interactions of 3A7MC can be responsible for biological properties [58]. The medium Raman band at 973 $cm^{-1}$ is attributed to C–O stretching mode, which is coupled with C–C stretching and C–H in plane bending mode. The C–C ring stretching vibrations have given rise to characteristic bands in both the observed IR and Raman spectra, covering the spectral range from 1610 to 1300 $cm^{-1}$. In 3A7MC, the ring mode manifests as a strong band in Raman and a weak band in infrared spectra at 1604 $cm^{-1}$, which is localized on the benzene part of the molecule. These vibrations corresponds to the $e_g$ mode (8a) of benzene [57] at 1610 $cm^{-1}$. The infrared band at 1572 and 1540 $cm^{-1}$ is attributed to C–C stretching. The weak IR bands at 1354 and 1279 $cm^{-1}$ are predominantly a C–C are predominantly a of benzene. The C–C stretching vibration at 1410 $cm^{-1}$ is coupled with the C–C–H bending modes, which can be inferred from results of PED calculations. The very strong band at 1248 $cm^{-1}$ in IR spectra is attributed to ring stretching mode of the benzene part. The ring stretching, in-plane, and out-of-plane bending vibrations have been identified and presented in Table 3. They also are in agreement with the literature [23–31].

*Low wavenumber vibrations of hydrogen bonds*

The attractive interaction between the hydrogen donor group and the acceptor moiety leads to the occurrence of new vibrational degrees of freedom, the so called hydrogen bond modes [59]. Such modes are connected with elongations changing the X···Y distance and/or the relative orientation of the hydrogen bonded groups. Thus, they provide direct insight into the structure of hydrogen bonds and into processes of bond formation and cleavage. As such modes are characterized by a high reduced mass of the oscillator and a small force constant determined by the comparably weak attractive interaction along the hydrogen bond, hydrogen bond modes occur at low wavenumbers in the range between 50–300 $cm^{-1}$. The low wavenumber bands of the hydrogen bond vibrations are generally found to be weak, broad and asymmetric in the Raman spectrum. The low wavenumber degrees of freedom such as librations as well as interaction-induced give rise to additional absorption and Raman bands that frequently overlap with the bands of the hydrogen bond modes. In addition, a substantial spread of vibrational wavenumber occurs for liquids with multiple hydrogen bonding geometries, resulting in a pronounced inhomogeneous broadening of the vibrational bands. The band in Raman at 82 $cm^{-1}$ has been attributed to a translational motion of the

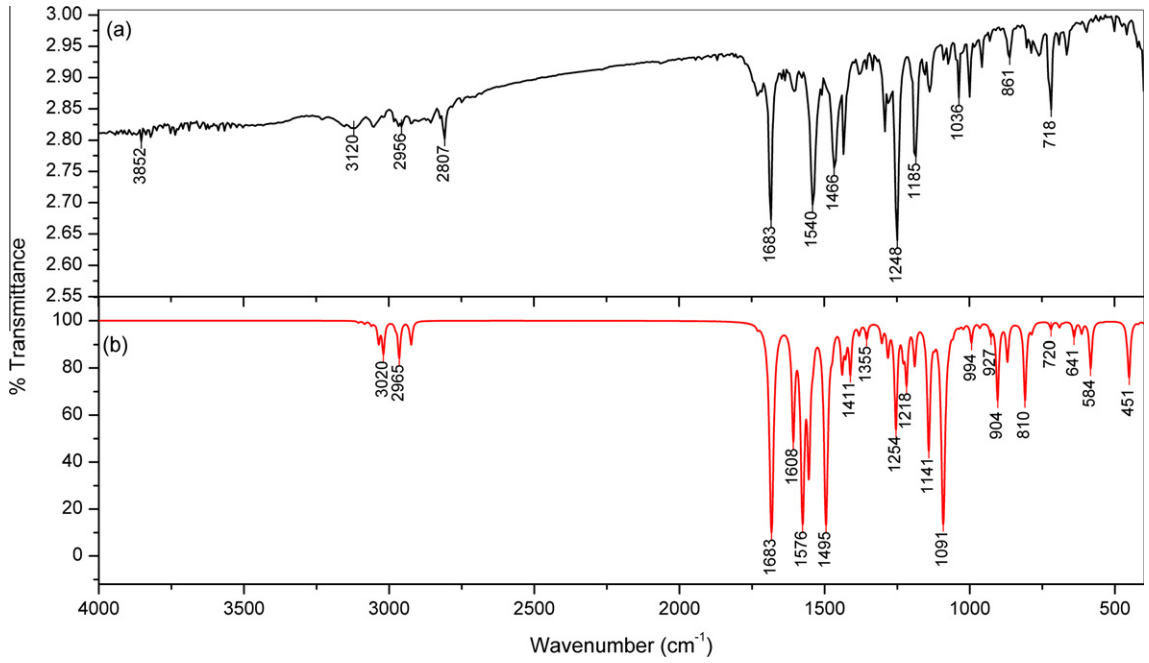


**Fig. 5.** (a) Experimental FT-IR spectra of 3-acetyl-7-methoxycoumarin in the range 4000–400 $cm^{-1}$ and (c) simulated IR spectra at the B3LYP/6-311G(d,p) level of theory.

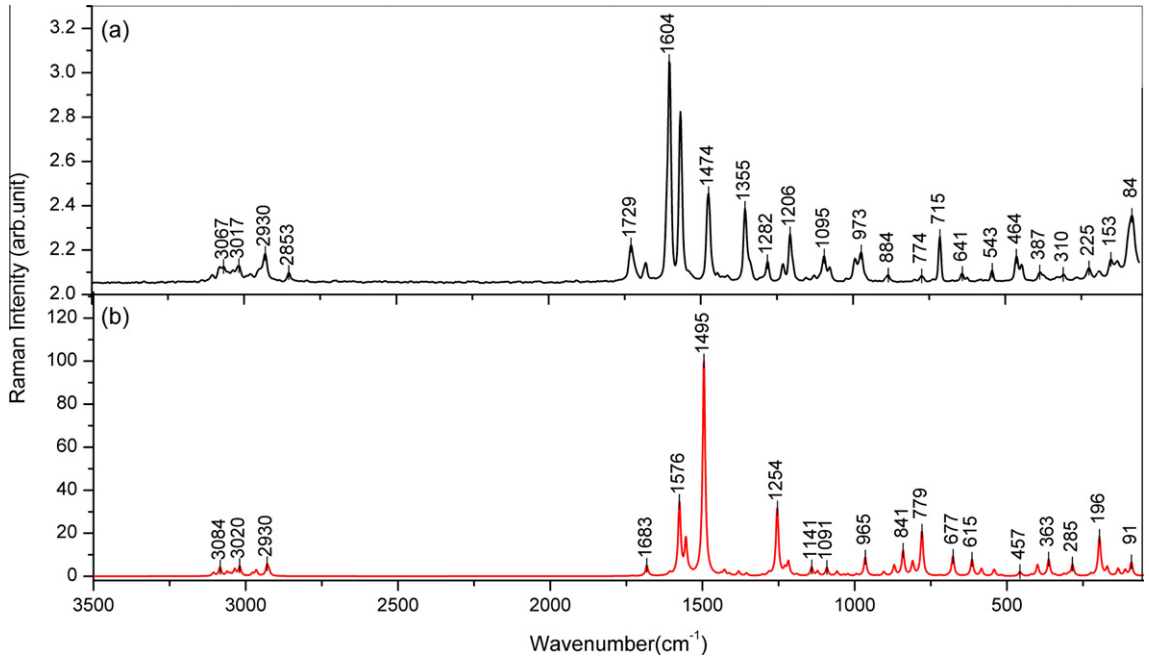


**Fig. 6.** (a) Experimental FT-Raman spectra of 3-acetyl-7-methoxycoumarin in the range 3500–100 $cm^{-1}$ and (b) simulated Raman spectra at B3LYP/6-311G(d,p) level of theory.

hydrogen bonded molecules including some bending component, the 182 $cm^{-1}$ band to a translational motion of the hydrogen bond. The lattice vibrations of rotatory type are generally stronger in intensity than the translatory type. The lattice modes in 3A7MC are found to be very intense in Raman compared with other modes in the high wavenumber region.

*UV–Vis spectral studies*

The UV–Vis spectra of 3A7MC molecule recorded in methanol solution are given in Supplementary S2. In an attempt to understand the nature of electronic transitions in terms of their energies and oscillator strengths, time-dependent DFT (TD–DFT) calculations involving configuration interaction between the singly excited electronic states were conducted on the molecule. Position and absorbance of the experimental peaks (Supplementary Figs. S2 and S3) together with the calculated transition energies, optical strengths, main configurations and mixing coefficients of the singlet ground and excited states and spectral assignments are given in Table S3. A close agreement has been obtained between the experimental and calculated values of transition energies.

TD-DFT calculations predict three transitions in the near ultraviolet region for 3A7MC molecule. The strong transitions at 274.4

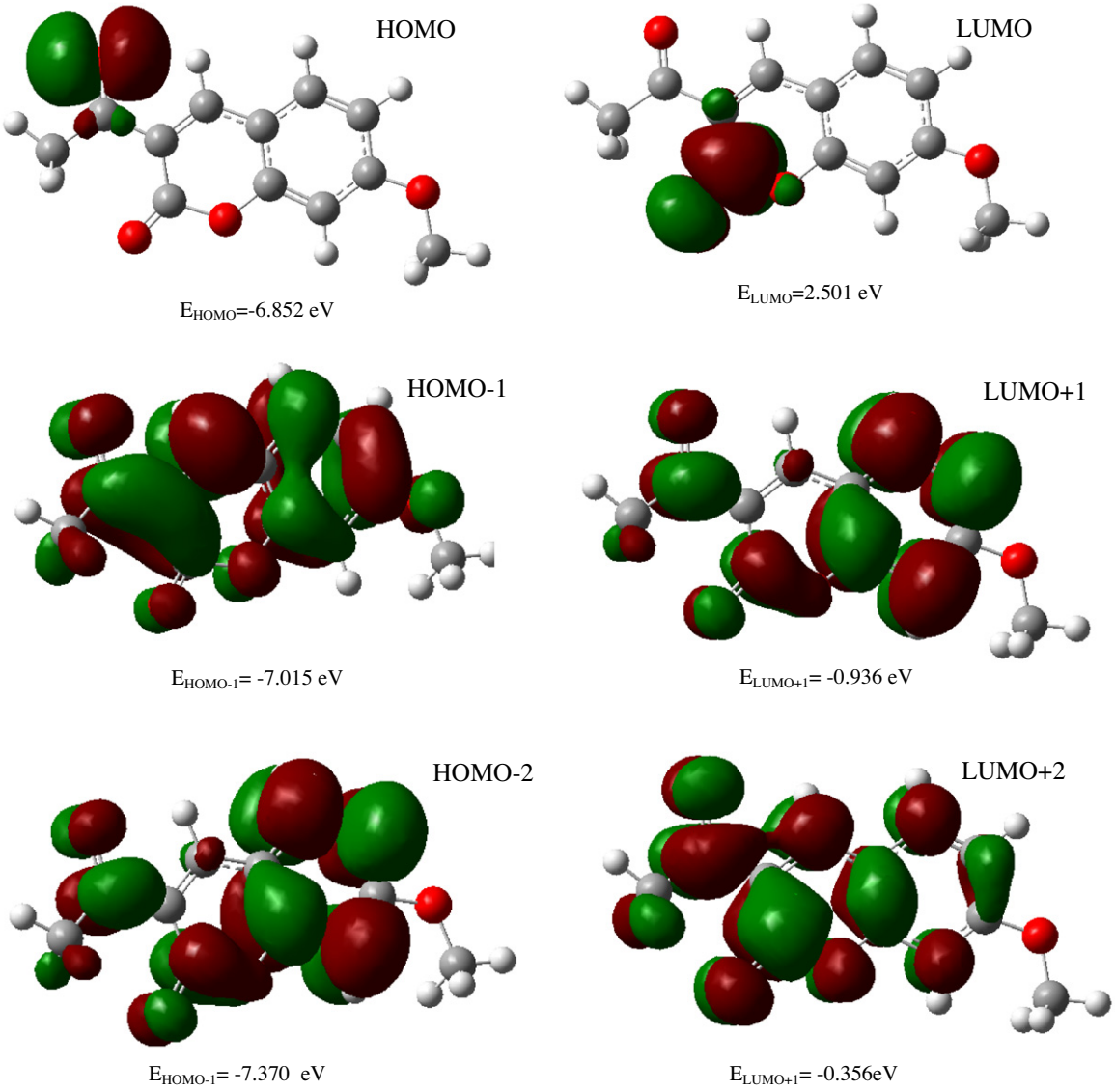


**Fig. 7.** HOMO and LUMO plot of 3-acetyl-7-methoxycoumarin by B3LYP/6-311G(d,p) level of theory.

(0.5681) and 179.48 (0.3989) nm have been observed at 300.8 and 239.0 nm, respectively, and are assigned to a $\pi$–$\pi^*$ transition (Supplementary Table S3). The numbers in parentheses represent oscillator strengths. On the basis of TD-DFT calculations, this shift may be explained as arising out of a larger decrease in the energy of the LUMO orbital (2.501 eV) than the HOMO (−6.852 eV) and the HOMO-1 (−7.015 eV) orbitals, relative to their positions in 3A7MC molecule.

The energy of the LUMO is directly related to the electron affinity and characterizes the susceptibility of the molecule towards attack by nucleophiles [60]. An electron affinity (EA) refers to the capability of a legend to accept precisely one electron from a donor. However, to influence the interacting systems, covalent or hydrogen bonding may take place which can result in a partial charge transfer [61]. A current approximation is to use Koopman's theorem to express these quantities in terms of the frontier one electron energy levels: HOMO and LUMO [62–65]. The energy of the HOMO is directly related to the ionization potential (IP) and characterizes the susceptibility of the molecules towards attack by electrophiles. Hard nucleophiles have a low HOMO energy while hard electrophiles have a high LUMO energy [60]. The operational definition of LUMO and HOMO in the context of DFT can be written as:

$$EA = -\xi LUMO \quad (3)$$

$$IP = -\xi HOMO \quad (4)$$

where $\xi HOMO$ and $\xi LUMO$ correspond to the Kohn Sham [66] one electron eigen values associated to the frontier molecular orbital: HOMO and LUMO, respectively. IP and EA refer to ionization potential and electron affinity of the system respectively. The HOMO–LUMO energy values of 3A7MC are shown in Fig. 7. HOMO–LUMO energy gap is used as a quantum chemical descriptor in establishing correlations for chemical and biochemical systems [67]. A large HOMO–LUMO gap implies high stability for the molecules in the sense of its lower charge transfer in complexes. Polarizability is another characteristic property which is related to HOMO–LUMO energy gap. Soft molecules with small energy gap will be more polarizable than hard molecules. The comparatively lower value of the $E_{LUMO}$-$E_{HOMO}$ (Fig. 7) of 3A7MC shows that the molecule is polarizable and biologically active [68]. The HOMO is located on the $C_{18}$═$O_2$ bonds of the acetyl group. The LUMO in 3A7MC,

however, populates on the lactone part, with only minor population on the $O_1$ and $C_6$ atoms .The population of LUMO on the bonding between $C_5 \equiv O_4$ forms antibonding orbitals. Minor population can be located on the $O_1$ and $C_6$ atoms. The difference between the orbital energies corresponding to HOMO-1(−7.015 eV) and HOMO-2 (−7.370 eV) is much higher than 0.05 eV indicating that the HOMO-1 and HOMO-2 are nondegenerate in 3A7MC. Similar conclusion can be drawn from the LUMO + 1 and LUMO + 2 orbital energy calculations.

*Molecular electrostatic potential*

The molecular electrostatic potential (ESP) at a point $r$ in the space around a molecule is (in atomic units)

$$V(r) = \sum_A \frac{Z_A}{|R_A - r|} - \int \frac{\rho(r)dr'}{|r'-r|} \quad (5)$$

$Z_A$ is the charge on nucleus $A$ located at $R_A$ and $\rho(r)$ is the electron density. The first term in the expression represents the effect of the nuclei and the second represents that of electrons. The two terms have opposite signs and therefore opposite effects. $V(r)$ is their resultant at each point $r$; it is an indication of the net electrostatic effect produced at the point $r$ by the total charge distribution (electrons + nuclei) of the molecule. Electrostatic potential correlates with dipole moment, electronegativity, partial charges and site of chemical reactivity of the molecule. It provides a visual method to understand the relative polarity of a molecule. While the negative electrostatic potential corresponds to an attraction of the proton by the concentrated electron density in the molecule (and is colored in shades of red on the ESP surface), the positive electrostatic potential corresponds to repulsion of the proton by atomic nuclei in regions where low electron density exists and the nuclear charge is incompletely shielded (and is colored in shades of blue). By definition, electron density isosurface is a surface on which molecule's electron density has a particular value and that encloses a specified fraction of the molecule's electron probability density. The electrostatic potential at different points on the electron density isosurface is shown by coloring the isosurface with contours. The graphical representation of the molecular electrostatic potential surface (MEP or ESP), as described by Politzer and Truhlar [69] is a series of values representing the evaluation of the interaction energy between a positively charged (proton) probe and points on a solvent accessible surface as defined by Connolly [70–72].

The electron density isosurface onto which the electrostatic potential surface has been mapped is shown in Figs. 8a–8c for 3A7MC. Such surfaces depict the size, shape, charge density and site of chemical reactivity of the molecules. The different values of the electrostatic potential at the surface are represented by different colors; red represents regions of most negative electrostatic potential, blue represents regions of most positive electrostatic potential and green represents regions of zero potential. Potential increases in the order red < orange < yellow < green < blue. Two projections of the ESP surfaces – one in molecular plane and in perpendicular planes – in the case of 3A7MC are shown in Figs. 8a and 8b. These projections clearly show a nucleophilic region sandwiching the π-system, leaving a more electrophilic region in the plane of the hydrogen atoms. In the case of 3A7MC molecule (Figs. 8a and 8b), which contain polar oxygen atoms, the shape of the electrostatic potential surface is influenced by the stereo structure and charge density distributions in the molecules with sites close to the oxygen atom of the acetyl group and the carbonyl group showing regions of most negative electrostatic potential. The ED plot for molecule shows a uniform distribution (Fig. 8c).

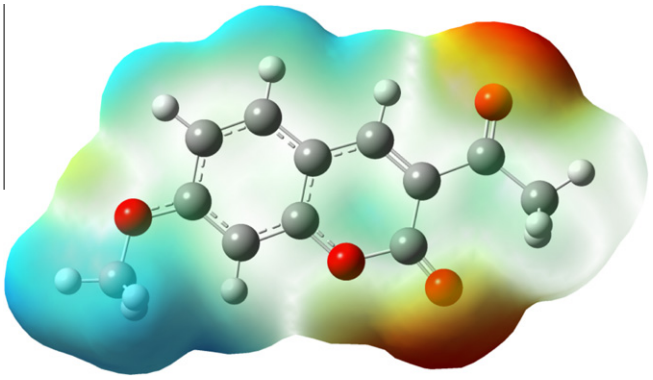

**Fig. 8a.** Molecular electrostatic potential mapped on the $\rho(r) = 0.0004$ a.u. isodensity surface for 3-acetyl-7-methoxycoumarin in the range from −5.644E-2 (red) to +5.644E-2 (blue).

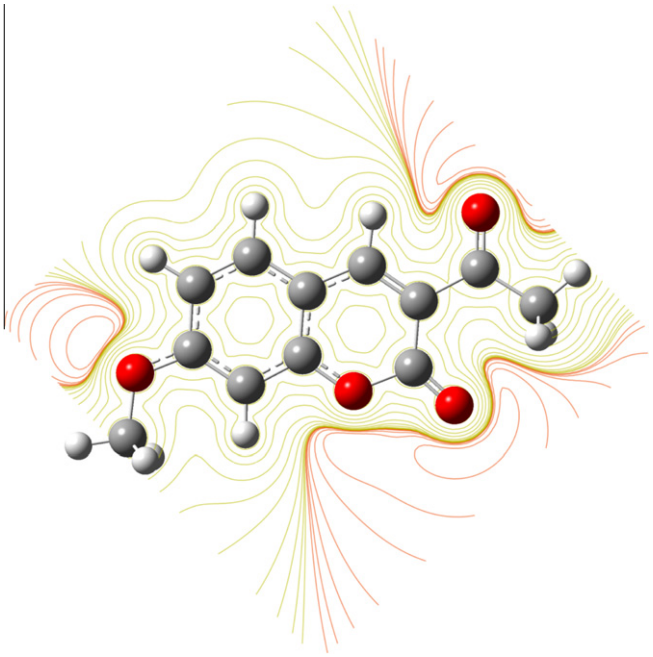

**Fig. 8b.** Molecular electrostatic potential mapped on the $\rho(r) = 0.0004$ a.u. isodensity surface for 3A7MC.

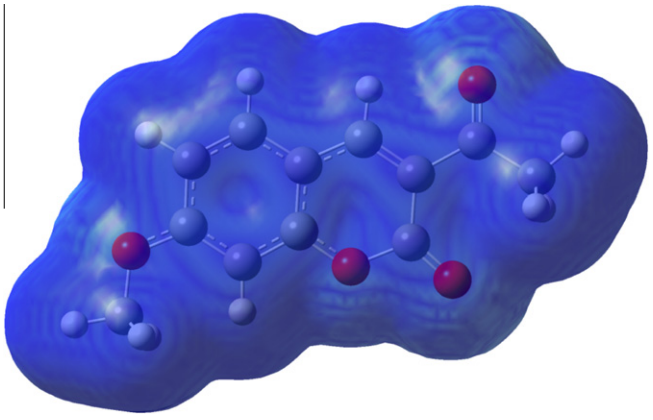

**Fig. 8c.** Electron density of 3-acetyl-7-methoxycoumarin molecule calculated at the B3LYP/6-311G(d,p) level of theory (For interpretation of the references to colour in this figure legend, the reader is referred to the web version of this article.).

## Conclusion

FT-IR and FT-Raman spectra of the 3-acetyl-7-methoxycoumarin have been recorded and analyzed. The gas phase structure and conformational properties of 3-acetyl-7-methoxycoumarin (3A7MC) and its conformers were determined by quantum chemical calculations. It is found that molecule has four conformations. Complete vibrational analysis of the most stable conformer of 3A7MC were performed according to the SQM force field method based on DFT calculations at B3LYP/6-311G(d,p) level. The conformer-1 of 3A7MC with torsion angle 0°, for $C_{15}$–$C_{14}$–$O_3$–$C_{23}$ and $C_5$–$C_6$–$C_{18}$–$C_{19}$ is found to be the most stable. The observed vibrational wavenumbers and optimized geometric parameters were seen to be in good agreement with the experimental data. Characteristic vibrational bands of the pyrone ring and methoxy and carbonyl groups have been identified. The lowering of HOMO–LUMO energy gap clearly explains the charge transfer interactions taking place within the molecule. Information regarding the size, shape, charge density distribution and sites of chemical reactivity of the presently studied molecule has been obtained by mapping electrostatic potential surface (ESP) on the electron density isosurface. Two projections of these maps in 3A7MC molecule, one in molecular plane and one in perpendicular planes, show a nucleophilic region sandwiching the π-system, leaving a more electrophilic region in the plane of the hydrogen atoms. In the case of 3A7MC molecule which contains polar oxygen atoms, the shape of the electrostatic potential surface is influenced by the stereo structure and charge density distributions. Sites close to the acetyl group and the carbonyl group show regions of most negative electrostatic potential.

## Acknowledgments

The author Lynnette Joseph would like to thank the University Grants Commission, New Delhi for its financial support, Project number: MRP(S)-899/10-11/KLKE002/UGC-SWRO. One of the authors (Y. Erdogdu) would like to thank Ahi Evran University Research Fund for its financial support, Project numbers: FBA-11-09.

## Appendix A. Supplementary data

Supplementary data associated with this article can be found, in the online version, at http://dx.doi.org/10.1016/j.saa.2012.07.084.

## References

[1] D. Sajan, Y. Erdogdu, R. Reshmy, Ö. Dereli, K. Kurien Thomas, I. Hubert Joe, Spectrochim. Acta 82 (2011) 118.
[2] J.W. Suttie, Clin. Cardiol. 13 (1990) 16.
[3] A.H. Bedair, N.A. El-Hady, M.S. Abd El-Latif, A.H. Fakery, A.M. El-Agrody, I1 Farmaco 55 (2000) 708.
[4] T. Patonay, G. Litkei, R. Bognar, J. Eredi, C. Miszti, Pharmazie 39 (1984) 86.
[5] C. Gnerre, M. Catto, F. Leonetti, P. Weber, P.A. Carrupt, C. Altomare, A. Carotti, B.J. Testa, Med. Chem. 43 (2000) 4747.
[6] D.A. Egan, P. James, D. Cooke, R. O'Kennedy, Cancer Lett. 118 (1997) 201.
[7] E. Budzisz, B.K. Keppler, G. Giester, M. Wozniczka, A. Kufelnicki, B. Nawrot, Eur. J. Inorg. Chem. (2004) 4412.
[8] M. Jiménez, J.J. Mateo, R. Mateo, J. Chromatogr. 870 (2000) 473.
[9] J. Koshy, V.G. Kumar Das, S. Balabaskaran, S.W. Ng, N. Wahab, Met. Based Drugs 7 (2000) 245.
[10] G.J. Finn, E. Kenealy, B.S. Creaven, D.A. Egan, Cancer Lett. 183 (2002) 61.
[11] B. Thati, A. Noble, B.S. Creaven, M. Walsh, M. McCann, K. Kavanagh, M. Devereux, D.A. Egan, Cancer Lett. 248 (2007) 321.
[12] B.M.W. Ouahouo, A.G.B. Azebaze, M. Meyer, B. Bodo, Z.T. Fomum, A.E. Nkengfack, Ann. Trop. Med. Parasitol. 98 (2004) 737.
[13] M. del Rayo Camacho, J.D. Phillipson, S.L. Croft, V. Yardley, P.N. Solis, Planta Med. 70 (2004) 70.
[14] G.J. Finn, B. Creaven, D.A. Egan, Melanoma Res. 11 (2001) 461.
[15] H. Itokawa, Y. Yun, H. Morita, K. Takeya, S. Rae Lee, Nat. Med. 48 (1994) 334.
[16] J.T. Brett, J.M. Alexander, J.J. Stezowski, J. Chem. Soc. Perkin Trans. 2 (2000) 1095.
[17] K. Vishnumurthy, T.N. Guru Row, K. Venkatesan, Observations on the Photochemical Behavior of coumarins and related systems in the crystalline state in understanding and manipulating excited-state processes, in: V. Ramamurthy, K.S. Schanze (Eds.), Molecular and Supramolecular Photochemistry, vol. 8, Taylor & Francise e-Library, New York, 2001.
[18] N.A. Nemkovich, H. Reis, W. Baumann, J. Lumin. 71 (1997) 255.
[19] V.K. Sharma, P.D. Saharo, N. Sharma, R.C. Rastogi, Spectrochim. Acta 59 (2003) 1161.
[20] S. Sardari, Y. Mori, K. Horita, R.G. Micetich, S. Nishibe, M. Daneshtalab, Bioorg. Med. Chem. 7 (1999) 1933.
[21] M.B. Maria, Z.Y. Wang, Tetrahedron Lett. 41 (2000) 4025.
[22] K.A. Thaker, D.D. Goswami, D.G. Pachpor, J. Indian Chem. Soc. 50 (1973) 420.
[23] V. Sortur, J. Yenagi, J. Tonannavar, V.B. Jadhav, M.V. Kulkarni, Spectrochim. Acta 64A (2006) 301.
[24] J. Tonannavar, Jayashree Yenagi, Veenasangeeta Sortur, V.B. Jadhav, M.V. Kulkarni, Spectrochim. Acta 77A (2010) 351.
[25] Anuradha Ramoji, Jayashree Yenagi, J. Tonannavar, V.B. Jadhav, M.V. Kulkarni, Spectrochim. Acta 77A (2010) 1039.
[26] A. Ramoji, J. Yenagi, J. Tonannavar, V.B. Jadhav, M.V. Kullarni, Spectrochim. Acta 68A (2007) 504.
[27] V. Arjunan, N. Puviarasan, S. Mohan, P. Murugesan, Spectrochim. Acta 67A (2007) 1290.
[28] E. Vogel, A. Gbureck, W. Kiefer, J. Mol. Struct. 177 (2000) 550.
[29] Sita Ram Tripati, Nitish K. Sanyal, Ind. J. Phys. 63B (1989) 474.
[30] V. Sortur, J. Yenagi, J. Tonannavar, V.B. Jadhav, M.V. Kulkarni, Spectrochim. Acta 71A (2008) 688.
[31] V. Arjunan, N. Puviarasan, S. Mohan, P. Murugesan, Spectrochim. Acta 67 (2007) 1290.
[32] A. Barzegar, M.D. Davari, N. Chaparzadeh, N. Zarghami, J.Z. Pedersen, S. Incerpi, L. Saso, A.A. MoosaviMovahedi, Iran. Chem. Soc. 8 (2011) 973.
[33] M. Yamaji, K. Nozaki, X. Allonas, S. Nakajima, S. Tero-Kubota, B. Marciniak, J. Phys. Chem. 113 (2009) 5815.
[34] R.M. Christie, Chih-Hung Lui, Dyes Pigm. 42 (1999) 85.
[35] M.S.A. Abdel-Mottaleb, B.A. Sayed, M.M. Abo-Aly, M.Y. El-Kady, J. Photochem. Photobiol. 46 (1989) 379.
[36] H.M. Han, C.R. Lu, Y. Zhang, D.C. Zhang, Acta Cryst. E61 (2005) 1864.
[37] H. Valizadesh, A. Shockravi, H. Gholipur, J. Heterocycl. Chem. 44 (2007) 867.
[38] M.J. Frisch, G.W. Trucks, H.B. Schlegel, G.E. Scuseria, M.A. Robb, J.R. Cheeseman, J.A. Montgomery Jr., T. Vreven, K.N. Kudin, J.C. Burant, J.M. Millam, S.S. Iyengar, J. Tomasi, V. Barone, B. Mennucci, M. Cossi, G. Scalmani, N. Rega, G.A. Petersson, H. Nakatsuji, M. Hada, M. Ehara, K. Toyota, R. Fukuda, J. Hasegawa, M. Ishida, T. Nakajima, Y. Honda, O. Kitao, H. Nakai, M. Klene, X. Li, J.E. Knox, H.P. Hratchian, J.B. Cross, C. Adamo, J. Jaramillo, R. Gomperts, R.E. Stratmann, O. Yazyev, A.J. Austin, R. Cammi, C. Pomelli, J.W. Ochterski, P.Y. Ayala, K. Morokuma, G.A. Voth, P. Salvador, J.J. Dannenberg, V.G. Zakrzewski, S. Dapprich, A.D. Daniels, M.C. Strain, O. Farkas, D.K. Malick, A.D. Rabuck, K. Raghavachari, J.B. Foresman, J.V. Ortiz, Q. Cui, A.G. Baboul, S.Clifford, J. Cioslowski, B.B. Stefanov, G. Liu, A. Liashenko, P. Piskorz, I. Komaromi, R.L. Martin, D.J. Fox, T. Keith, M.A. Al-Laham, C.Y. Peng, A. Nanayakkara, M. Challacombe, P.M.W. Gill, B. Johnson, W. Chen, M. W. Wong, C. Gonzalez, J.A. Pople, Gaussian 03, Revision C.02, Gaussian, Inc., Wallingford, CT, 2004.
[39] J. Baker, A.A. Jarzecki, P. Pulay, J. Phys. Chem. 102 (1998) 1412.
[40] P. Pulay, G. Fogarasi, F. Pang, J.E. Boggs, J. Am. Chem. Soc. 101 (1979) 2550.
[41] T. Sundius, J. Mol. Struct. 218 (1990) 321.
[42] T. Sundius, Vib. Spectrosc. 29 (2002) 89.
[43] G. Keresztury, S. Holly, J. Varga, G. Besenyei, A.Y. Wang, J.R. Durig, Spectrochim. Acta 49 (1993) 2007.
[44] H.W. Thomson, P. Torkington, J. Chem. Soc. 171 (1945) 640.
[45] E.D. Glendening, J.K. Badenhoop, A.E. Reed, J.E. Carpenter, J.A. Bohmann, C.M. Morales, F. Weinhold, NBO 5.0, Theoretical Chemistry Institute, University of Wisconsin, Madison, 2001.
[46] F. Weinhold, Nature 411 (2001) 539.
[47] F. Weinhold, C. Landis, Valency and Bonding: A Natural Bond Orbital Donor–Acceptor Perspective, Cambridge University Press, Cambridge, 2005.
[48] G. Rauhut, P. Pulay, J. Phys. Chem. 99 (1995) 3093.
[49] D.N. Sathyanarayana, Vibrational Spectroscopy Theory and Applications, New Age International Publishers, New Delhi, 2004.
[50] L.J. Bellamy, Infrared Spectroscopy of Complex Molecules, Methuen, London, 1954.
[51] N.B. Colthup, L.H. Daly, S.E. Wiberley, Introduction to Infrared and Raman Spectroscopy, Academic Press, New York, 1990.
[52] B.C. Smith, Infrared Spectral Interpretation, CRC Press, Boca Raton, FL, 1996.
[53] G. Socrates, Infrared Characteristic Group Frequencies, Wiley–Interscience Publication, 1980.
[54] Y. Erdogdu, M.T. Güllüoğlu, Spectrochim. Acta 74 (2009) 162.
[55] N.P.G. Roeges, A Guide to the Complete Interpretation of Infrared Spectra of Organic Structures, Wiley, New York, 1994.
[56] M. Gussoni, C. Castiglioni, J. Mol. Struct. 521 (2000) 1.
[57] G. Varsanyi, Vibrational Spectra of Benzene Derivatives, Academic Press, New York, 1969.
[58] R. Filler, R. Saha, Future Med. Chem. 5 (2009) 777.
[59] T.J. Erik, Nibbering Thomas Elsaesser, Chem. Rev. 104 (2004) 1087.
[60] M. Karelson, V.S. Lobanov, Chem. Rev. 96 (1996) 1027.
[61] P. Thanikaivelan, V. Subramanian, V.R. Raghava, B.N. Unni, Chem. Phys. Lett. 323 (2000) 59.
[62] R. Contreras, P. Fuentealba, M. Galvan, P. Perez, Chem. Phys. Lett. 304 (1999) 405.
[63] P. Fuentealba, R. Contreras, Reviews of Modern Quantum Chemistry, in: K.D. Sen (Ed.), World Scientific, Singapore, 2002 (vol. II).

[64] P. Fuentealba, P. Perez, R. Contreras, J. Chem. Phys. 113 (2000) 2544.
[65] I. Fleming, Frontier Orbitals and Organic Chemical Reactions, John Wiley and Sons, New York, 1976.
[66] W. Kohn, L. Shan, J. Phys. Rev. 140 (1965) 1133.
[67] N. Francisco, V. Ricardo, J. Mol. Struct. 850 (2008) 127.
[68] L. Padmaja, C. Ravikumar, D. Sajan, I. Hubert Joe, V.S. Jayakumar, G.R. Pettit, O. Faurskov Nielsen, J. Raman Spectrosc. 40 (2009) 419.
[69] P. Politzer, D.G. Truhlar (Eds.), Chemical Applications of Atomic and Molecular Electrostatic Potentials, Plenum Press, New York, 1981.
[70] B. Chattopadhyay, S. Basu, P. Chakraborty, S.K. Choudhuri, A.K. Mukherjee, M. Mukherjee, J. Mol. Struc. 932 (2009) 90.
[71] U.C. Singh, P.A. Kollman, J. Comput. Chem. 5 (1984) 129.
[72] M.L. Connolly, Science 221 (1983) 709.